

AN ABSTRACT OF THE THESIS OF

Guangyuan Liang for the degree of Master of Science in Materials Science presented on November 25, 2019

Title: Synthesis and Characterization of an Ultrafine-Grained Aluminum-Copper System through High-Pressure Torsion

Abstract approved:

Megumi Kawasaki

Aluminum and copper and their alloys have been widely used due to relatively high strength-to-weight ratios compared with conventional steels. Processing of these alloys is typically conducted at high temperatures over extended time periods. High-pressure torsion (HPT) is a promising processing technique for introducing significant grain refinement leading to excellent mechanical properties, such as strength and ductility, in bulk metals and alloys at ambient temperatures. In the present study, in addition to the principle of grain refinement, HPT was applied for synthesizing a hybrid metal system of an Al-Cu alloy. In practice, an Al-1050 alloy and a commercial purity Cu were processed concurrently by HPT under a compressive pressure of 6.0 GPa at a rotational speed of 1 rpm for up to 60 rotations. The evolution in microstructure and the formation of intermetallic compounds were observed by scanning electron microscopy, energy dispersive X-ray spectroscopy and X-ray diffraction analysis. Hardness measurements demonstrated heterogeneous distributions of hardness from the disk centers to the edges, thereby suggesting a formation of microstructural heterogeneity. This study demonstrates the feasibility of HPT processing for introducing a wide range of unique metal systems.

©Copyright by Guangyuan Liang
November 25 2019
creative commons license

Synthesis and Characterization of an Ultrafine-Grained Aluminum-Copper System
through High-Pressure Torsion

by
Guangyuan Liang

A THESIS

submitted to

Oregon State University

in partial fulfillment of
the requirements for the
degree of

Master of Science

Presented November 25 2019
Commencement June 2020

Master of Science thesis of Guangyuan Liang presented on November 25, 2019

APPROVED:

Major Professor, representing Material Science

Director of the Materials Science Program

Dean of the Graduate School

I understand that my thesis will become part of the permanent collection of Oregon State University libraries. My signature below authorizes release of my thesis to any reader upon request.

Guangyuan Liang, Author

ACKNOWLEDGEMENTS

The author expresses sincere appreciation to Dr Kawasaki for her support and encouragement throughout the writing.

TABLE OF CONTENTS

	<u>Page</u>
1 Introduction.....	1
2 Literature Review.....	3
2.1 Ultrafine Grained Materials.....	3
2.2 Severe Plastic Deformation.....	6
2.3 High Pressure Torsion	8
2.4 Mechanical Bonding of Dissimilar Metals by HPT.....	12
3 Experimental Procedures	15
3.1 Materials Processing	15
3.2 Characterization	16
3.3 Collaboration work Nanoindentation.....	17
4 Results	18
4.1 Microstructure: Overview.....	18
4.2 Hardness along Disk Diameter.....	20
4.3 Elemental Analysis	24
4.4 X-ray Diffraction.....	25
4.5 Nano-indentation	28
5 Discussion.....	31
5.1 Significant strengthening by HPT.....	31
5.2 Homogeneity of Hardness	34
5.3 Specific Strength.....	35
5.4 Strain rate sensitivity.....	37

TABLE OF CONTENTS (Continued)

	<u>Page</u>
6 Summary and Conclusions.....	38
7 Future Work	39
Bibliography	40

LIST OF FIGURES

<u>Figure</u>	<u>Page</u>
2.1 Conventional strength vs ductility plot.....	4
2.2 Schematic of decreasing grainsize vs mechanical properties	5
2.3 Updated strength vs ductility plot with HPT materials.....	7
2.4 Schematic illustration of various HPT types.....	8
2.5. Schematic illustration of HPT disk.....	9
2.6 Optical micrograph of polished and etched Al HPT disk.....	10
2.7 3-D plot of hardness vs position of HPT Al 1050 disk.....	11
2.8 Hardness vs disk radius and applied pressure of HPT Al 1050 disk.....	11
2.9 Schematic and photos of semi-circle HPT hybrid disk system.....	13
2.10 Schematic, photos and simulation of quarter-circle HPT hybrid disk system.....	13
2.11 Schematic of quasi-constrained HPT.....	14
3.1 Photograph of HPT facility.....	15
4.1 Optical micrographs of Al-Cu vertical cross section.....	18
4.2 Optical micrographs of Al-Cu surface near mid-thickness.....	19
4.3 Vickers microhardness of Al-Cu disks at various turns.....	21
4.4 Vickers microhardness of Al-Cu disks near edge and mid thickness.....	22
4.5 Contour plots of Vickers microhardness of vertical cross sections.....	22
4.6 Summary of Al-Cu hardness vs pure Al and Cu.....	23
4.7 SEM and EDX of Al-Cu edge mixing.....	24
4.8 XRD patterns of Al-Cu 20 turns and 60 turns.....	26
4.9 XRD patterns of Al-Cu 60 turns edge and disk center.....	27

LIST OF FIGURES (Continued)

Figure	Page
4.10 Load displacement curves for Al-Cu 20 turns near disk edge.....	28
4.11 Load displacement curves for Al-Cu 60 turns near disk edge.....	29
5.1 Hardness vs equivalent strain of Al-Cu disks.....	32
5.2 Schematic of 3 variations of hardness evolutions after HPT processing.....	33
5.3 Strain rate sensitivity of Al-Cu nanoindentation measurements.....	37

LIST OF TABLES

<u>Table</u>		<u>Page</u>
4.1	Phase compositional results for Al-Cu 20 and 60 turns.....	26
4.2	Phase compositional results for Al-Cu 60 turns near edge and center.....	27
5.1	Specific strength of HPT Al Cu single alloy and hybrid	35

1 Introduction

Light-weight metal alloys are of great interest to structural manufacturing due to a combination of good strength and low weights. The properties are particularly desirable in the transportation industry, as low weights lead to less energy used as fuel. Aluminum (Al) and copper (Cu) and their alloys are of particular interest because of their abundance in nature. Moreover, copper has high electrical conductivity, thereby generating a high demand as conductive wires. Aluminum and copper alloys are commercially readily available and economic in scale, thus there would be few supply chain issues to use these for new applications.

Both Al and Cu have a face centered cubic crystal structure, which allows for dislocations to slip the fully dense family planes of 111 in 110 family directions during plastic flow. This gives these metals essentially reasonable ductilities and allows for easy forming. However, their strength in general is not comparable to other common structural materials such as steel, while non-ferrous metals and alloys including Al and Cu have much lighter densities than ferrous alloys.

Numerous studies have been conducted to improve the strength and hardness without losing ductility of these alloys by different processing techniques where typically these focus on a few strengthening mechanisms: strain hardening, solid solution strengthening and precipitation hardening. However, there is an upper limit on the improvements in these properties by processing a single metal due to the saturation in structural changes. In this context, bonding or cladding of dissimilar metals is an alternative approach for improving mechanical properties dramatically. In particular, the formation of nano-scale intermetallic phases during the mechanical bonding can stabilize the microstructure from recovery at a wide range of temperature while strengthening the materials.

Conventional thermo-mechanical processing of rolling requires high temperatures for long durations for the mechanical bonding of dissimilar metals and often introduce microstructural anisotropy within the materials in rolling, transverse and normal directions. While this approach does ultimately achieve reasonable mixing of dissimilar metal phases and improved strength, there is a high cost in energy, from high-temperature processing, and requires a long processing time. By

contrast, using severe plastic deformation (SPD) techniques, mechanical bonding can be achieved in a relative short period of time at near room temperature. Another benefit of SPD is the higher levels of grain refinement, which accelerated atomic diffusion and the activity of grain boundary sliding as a deformation mechanism and potentially allowing for better ductility. Processing by High-Pressure Torsion (HPT) is considered as the best SPD method in terms of grain refinement and in fact this produces enable to introduce finer grains than other SPD bulk metal processes. The HPT system can apply high compressive force for introducing severe hydrostatic pressure and concurrent torsional stress to process ultrafine-grained metals and alloys with superior strength.

Accordingly, multiple metal samples can be applied to HPT and bonded mechanically during the grain refinement process at ambient temperature. Typically, when metals are strengthened, they become more brittle and it is described as a paradox of strength and ductility. However, with a combination of grain refinement and mechanical bonding of dissimilar metals through the application of HPT, the synthesized hybrid alloys can have ultrafine-grained microstructures leading to excellent mechanical priorities of both strength and ductility.

In the present study, Al and Cu in a disk shape are diffusion bonded by HPT for up to 60 turns (60 minutes process at 1 rpm) under a compressive pressure of 6.0 GPa at room temperature. The evolution of microstructure, phase composition and hardness and plasticity were evaluated by a series of the characterization techniques. Special emphasis is placed for demonstrating the significance of HPT processing for successful diffusion bonding of dissimilar metals and alloys and an improvement of hardness and specific strength by potentially synthesizing intermetallic phases.

2 Literature Review

2.1 Ultrafine-Grained Materials

Grain refinement comes with numerous benefits including increased hardness, enhanced ductility, improved wear resistance and additional functionalities [1]. In general, thermomechanical processing, such as extrusion and cold/hot rolling, is applied for processing conventional engineering metals to have fine grain sizes of ~5-10 μm . The last two decades, significant efforts have been directed towards reducing the grain size of engineering metals and alloys for forming ultrafine-grained (UFG) microstructure with submicrometer grain sizes in a range of 100-1000 nm or even in the nanocrystalline level with grain sizes in a range of 10 to 100 nm. The top-down approach [2] is one of the attractive strategies used in metallurgy for producing bulk nanostructured materials (BNM), which involves refining coarse grains to ultrafine grains in the bulk solids. This approach for processing UFG materials and BNM is feasible by applying the techniques involving severe hydrostatic pressure, which introduces high population of lattice defects including vacancies and dislocations [2,3]. Accordingly, the application of severe plastic deformation has been studied as an effective technique to achieve such UFG microstructure in advanced engineering metals and alloys.

The Hall-Petch relationship in equation 2.1 models the yield strength of a material, σ_y , as a function of the average grain size, d [4,5]:

$$\sigma_y = \sigma_0 + k_y d^{-1/2} \quad (2.1)$$

where σ_0 is the lattice friction stress and k_y is the yielding constant. This relationship works most accurately at temperatures below $0.5 T_m$ where T_m is the absolute melting temperature of materials. Thus, this relationship suggests the reduction in grain size is effective to increase the strength of engineering metals. At elevated temperatures, UFG materials generally show superplastic ductility in tension due to the activation of grain boundary sliding [6]. In practice, superplasticity is a phenomenon in which a large elongation of $>400\%$ is acquired prior to fracture [7]. This situation is achieved when fulfilling the conditions associated with microscopic structure, generally at grain sizes smaller than 2-5 μm as well as temperature of $\geq 0.5 T_m$ and strain rates of

10^{-4} - 10^{-1} s $^{-1}$, in order to accelerate the dominant flow mechanism of grain boundary sliding (GBS). Thus, SPD techniques with an ability to introduce ultrafine grain sizes provide ideal materials for achieving superplastic ductility at elevated temperatures [8].

Metallic materials generally exhibit either strong but brittle or ductile but less strong, and these essential characteristics is labeled *the paradox of strength and ductility* as illustrated in Figure 2.1 [9] where yield stress is plotted against elongation to failure for a series of metallic materials including Cu and Al samples after conventional cold-rolling with several different strains. This plot appropriately summarizes the maxim noted in earlier reports that “materials may be strong or ductile, but rarely both at once” [10,11]. This plot includes two points indicated nano Ti and nano Cu where these nanostructured metals exhibit a combination of exceptional strength and ductility after processing by high-pressure torsion (HPT) [10] and by equal-channel angular processing (ECAP) [12], respectively. These earlier reports suggest that there is a potential to introduce both high strength and good ductility in UFG metals when processing through SPD to very large strains and thereby increasing the strain rate sensitivity leading to the occurrence of GBS [13].

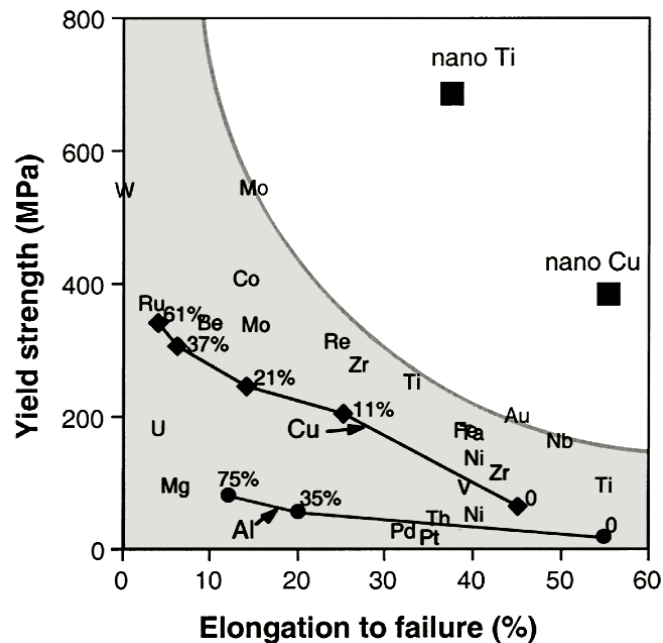


Figure 2.1 Conventional plot of yield stress against elongation to failure illustrating the paradox of strength and ductility for a series of metallic materials [9].

Figure 2.2 shows the general evolution in mechanical properties as a function of grain size for conventional metallic materials [14]. As suggested by the Hall-Petch relationship in equation (1), strength increases with reducing grain sizes. Although general thermomechanical processing may reduce or at most retain the ductility, as was also shown in Figure 2.1, processing of UFG materials by SPD techniques introduces significant amounts of point and line defects promoting during microstructural refinement [15,16]. This ultimately leads to the achievement of the combination of an increased rate of strain hardening and the increased value of strain rate sensitivity, m , thus accelerating GBS, in UFG materials at ambient temperatures. A high rate of strain hardening allows the dislocations to accumulate in the grains and the accelerated GBS delays the onset of necking. Thus, these mechanisms allow the material to exhibit a reasonable level of tensile ductility when strained, and combining with high strength SPD processing is feasible to introduce the UFG materials which will have improved toughness as shown in Figure 2.2.

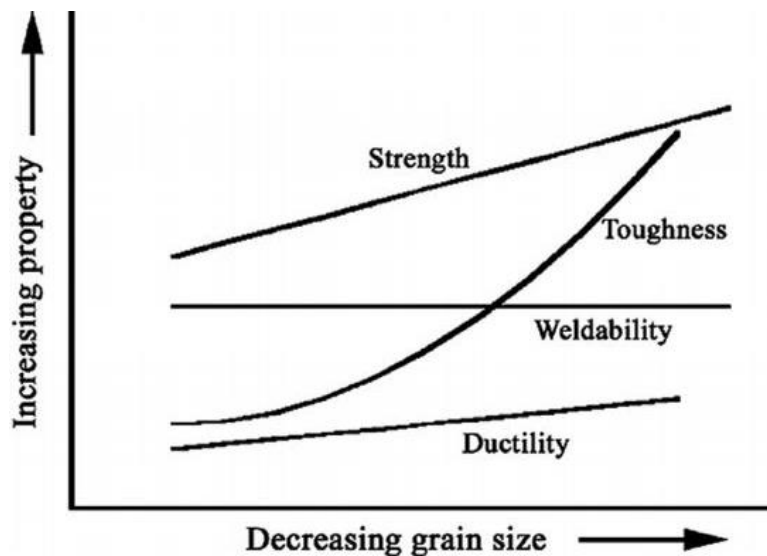


Figure 2.2 A schematic plot showing the effect of decreasing grain size on mechanical properties of metallic materials [14].

2.2 Severe Plastic Deformation

Various methods have been developed to process UFG materials, however a limited grain refinement has been achieved through conventional thermomechanical processes. Therefore, SPD processing has been studied for the last two decades to produce bulk UFG materials [3,17,18]. SPD processing is defined as the techniques which introduce severe plastic strain on materials and thereby significantly reducing the grain size. Generally, the material volume is maintained constant under significant hydrostatic pressure where the processing tools having special geometries are used to prevent free flow of the material so as to achieve extreme strains.

Among the numerous reports on the SPD techniques, ECAP and HPT have been applied extensively to produce a wide range of UFG materials [19]. In ECAP, the material is pressed through a solid die having a channel with an obtuse angle so that a high strain is induced as the sample is pushed through the corner of the channel introducing a simple shearing plane [12]. Since the sample dimensions can be maintained during processing, continuous pressings are applicable using the same sample [20]. Although the ECAP technique provides a capability of introducing excellent grain refinement and superior ductility [21], it produces microstructures consisting of grains within a submicrometer range even after multiple pressings.

Processing by HPT has become a reliable procedure in terms of producing bulk materials with true nano-scale grain sizes [22]. The processing procedure involves two large anvils where a disk-shaped material receives extreme compressive pressure and concurrent torsional straining by the concurrent movement of anvils. The detail procedure of HPT processing will be explained in the following section. Figure 2.3 shows a recent report demonstrating the overcoming of *the paradox of strength and ductility* for an Al-7%Si alloy processed by HPT [23]. Specifically, the experimental data of the achieved yield stress and elongation to failure of the HPT-processed Al-Si samples are superimposed in Figure 2.3. The dark red arrow indicates, as the anvil rotations, N , increase, the imposed strain by HPT to the material increases, and ultimately both the yield strength and elongation to failure were improved in the Al-Si alloy after HPT. Moreover, the improved ductility by the activated GBS was observed in the consistent Al-Si alloy processed by HPT [24].

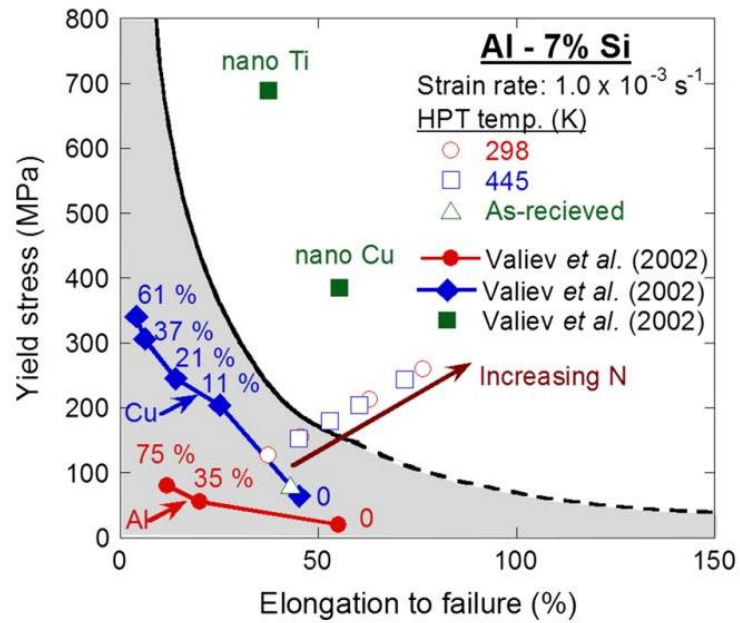


Figure 2.3 Using the conventional plot in Figure 2.1 to illustrate experimental datum points for the Al-7% Si alloy processed by HPT at 298 K [24]: the arrow shows the effect of increasing the numbers of turns in HPT [23]

2.3 High-Pressure Torsion

Nobel Laureate Professor P.W. Bridgman pioneered his work on the basics of the HPT technique as early as the 1930s [25], while only in the last two decades it has studied extensively to produce UFG materials. A comprehensive history of the HPT processing technique is available in a recent review [26]. In HPT, a thin disk is subjected to a high compressive pressure and concurrent torsional straining at often room temperature. Depending on the material and the processing conditions, this procedure can produce true nano-scale microstructure in bulk metals with grain sizes <100 nm. In practice, it is well defined that exceptional microstructural refinement is viable using HPT by comparison with other SPD procedures [27].

There are three types of HPT anvil configurations which have been developed and these are illustrated in Figure 2.4 [22]. Across all types, these sets of anvils apply high pressure to the disk samples and one of the anvils rotates at a steady rate. An unconstrained HPT facility as shown in Figure 2.4(a) allows the free flow of an excess volume of a material out of the pressing region and results in gradual thinning of the sample leading to a substantial loss of the material. To resolve these issues, the application of the constrained HPT anvils was developed as shown in Figure 2.4(b). The cylindrical wall of one of the anvil set greatly reduces a loss of the material and maintains the shape of the material. However, the constrained HPT facility causes an increased friction between the sample and the cylindrical wall. Therefore, the quasi-constrained HPT anvils as illustrated in Figure 2.4(c) were developed as an intermediate solution for imposing severe straining while limiting the outflow of the material volume, thus reasonably preserving the original sample volume.

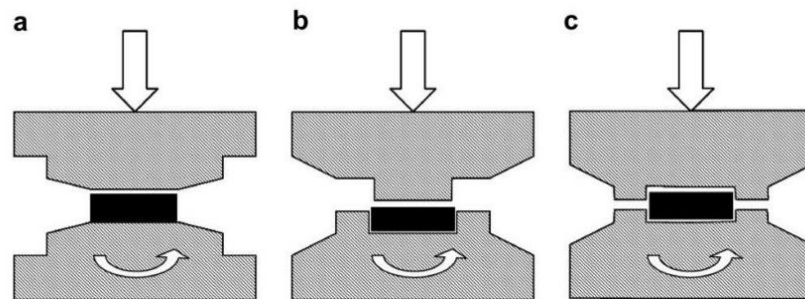


Figure 2.4 Schematic illustrations of the HPT anvils for (a) unconstrained, (b) constrained and (c) quasi-constrained conditions [22].

When a disk sample is processed by HPT, the torsional shear strain, γ , is given by the following form:

$$\gamma = \frac{2\pi Nr}{h} \quad (2.2)$$

where N is the number of anvil rotations, r is the radial distance from the disk center and h is the height of the disk sample. Figure 2.5 [25] shows a schematic of the principles of HPT processing where the amount of displacement (dl) varies depending on the disk radius, even if the angle of rotation ($d\theta$) is taken consistent. Then, the equivalent von Mises strain is modeled by equation 2.3 [27,28].:

$$\varepsilon_{eq} = \frac{2\pi Nr}{h\sqrt{3}} \quad (2.3)$$

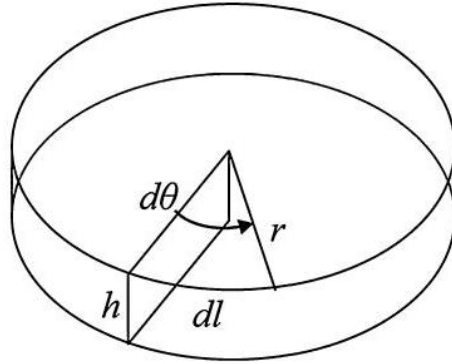


Figure 2.5 Schematic of parameters used to determine shear strain. [26]

Equations 2.2 and 2.3 suggest that the induced strain varies depending on the location along the disk radius and thus there is a significant strain heterogeneity across the sample diameter. Specifically, the equivalent strain at the disk center is zero and thus a minimal amount of strain hardening occurs while the highest straining is provided at the disk periphery. This strain heterogeneity by HPT was indirectly demonstrated by an earlier experiment, where a high purity Al (99.99%) was processed by HPT under 6.0 GPa for 1 rotation at a rotational speed of 1 rpm and the disk surface after slight polishing was shown in Figure 2.6 [29]. The micrograph shows a significant difference in microstructure between the center and the edge of the material after 1 HPT rotation.

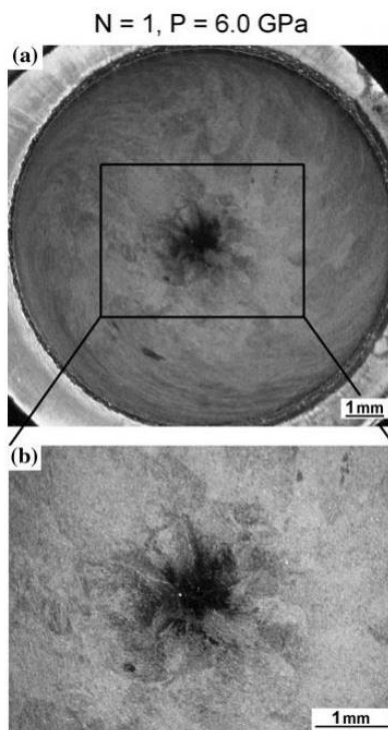


Figure 2.6 Optical micrographs showing (a) polished and etched surface of an Al-1050 alloy disk after HPT for 1 rotation at 6 GPa and (b) an increased magnification of the disk center [29].

On the contrary, after sufficient rotations by HPT, it is reported earlier that reasonably homogeneous microstructure can be achieved across the disk samples [30] and it is also indirectly measurable when examining the values of microhardness over the disk surfaces with increasing numbers of HPT rotations. An example is shown in Figure 2.7 for an Al-1050 alloy processed by HPT for (a) $\frac{1}{4}$ turn, (b) 1 turn and (c) 5 turns under 6.0 GPa [31]. There is an apparent hardness heterogeneity in an early stage of deformation after $\frac{1}{4}$ turn where low hardness at the disk center increases towards the disk edge of the Al alloy. With increasing numbers of HPT rotations, the lower hardness at the disk center develops and ultimately the hardness across the disk diameter achieves the maximum saturated value after 5 turns. Thus, it is summarized in an earlier review that the increasing numbers of HPT rotation enable to impose severe straining which is enough to refine the microstructure across the disk volume leading to homogeneously high hardness over the disk surfaces after enough numbers of HPT rotation of at least 5 turns [32].

In this context, it is also important to note that increasing compressive pressure also influences significantly to the homogeneity of microstructure and hardness. Figure 2.8 shows the variation of the Vickers Microhardness in (a) a radial distance under 1 and 9 GPa after 5 rotations and (b) the centers and edges under compressive pressures of 1-9 GPa by HPT for 5 turns in a Ni disk [33]. It is apparent that the higher pressure introduces a reasonable level of homogenous hardness, which indicates that the microstructure also achieves better homogeneity. These examples are representative of most metals and alloys processed by HPT, and a numerous study confirmed that high pressures of ~ 6.0 GPa and 5 or higher rotations are necessary to achieve reasonable microstructural homogeneity within the disk samples.

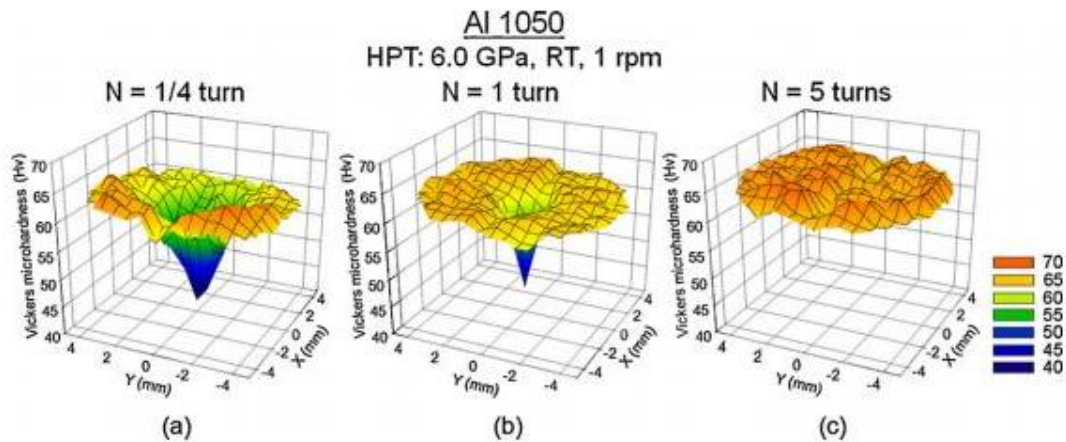


Figure 2.7 3D-view of Vickers microhardness vs position after (a) $1/4$, (b) 1, (c) 5 anvil rotations of an HPT processed 99.5% purity Al-1050 alloy [31].

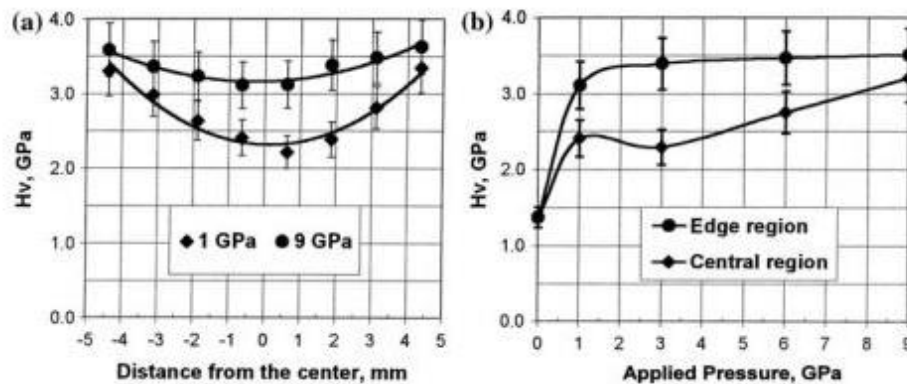


Figure 2.8 Vickers Microhardness vs (a) radial distance after 5 rotations (b) compressive pressure during HPT [33]

2.4 Mechanical Bonding of Dissimilar Metals by HPT

Due to an ability of extensive grain refinement at room temperature, the HPT processing has applied for the bonding of machining chips [34-36] and the consolidation of metallic powders [37-46]. Moreover, another strategy of the use of HPT processing is developed for mechanically bonding of dissimilar metals and alloys while significant grain refinement is anticipated during the procedure. A very first demonstration of the mechanical bonding by HPT was shown in Figure 2.9 where two semi-circle disks of Al and Cu were placed together to form a complete disk shape and processed under HPT for 6 GPa for up to 100 anvil rotations [47]. This study reported the bonding of these dissimilar metals as well as the formation of intermetallic Al_2Cu and Al_4Cu_9 phases. A similar study involving four quarter-circle disks of an Al-6061 alloy and a commercial purity Cu was shown for mechanical bonding by HPT as shown in Figure 2.10 [48] where (a) the schematic and (b) the actual sample set-up of the four quarter-circle disks were processed at 2.5 GPa for 1 rotation at room temperature for architecturing of spiral microstructure which is computationally calculated as shown in Figure 2.10 (c) and (d).

Based on these earlier studies, further effective mechanical bonding by increasing interfacial regions of the dissimilar metals has been studied and the first example was shown in Figure 2.11 [49]. In practice, three separate disks of a commercial purity Al and a Mg alloy, ZK-60, were stacked in the order of Al/Mg/Al and processed under 6.0 GPa for up to 10 rotations [49] and 20 rotations [50] at room temperature. This unique sample set-up using the conventional HPT facility has attracted much attention for the efficient mechanical bonding of dissimilar metals at room temperature. Accordingly, the consistent technique of the mechanical bonding of two dissimilar metal disks by HPT was applied for forming a bi-layered microstructure of an Al-Mg system by stacking two disks of Al and Mg and processing at 6.0 GPa for up to 20 turns [51]. Moreover, the mechanical bonding of alternately stacked 19 Cu and 18 Ta thin foils led to form a bulk solid under 4.0 GPa for up to 150 turns [52]. Thus, the present research applies the consistent sample set-up as shown in Figure 2.11 on two dissimilar metals of Al and Cu alloys to mechanically bond and form an Al-Cu hybrid alloy system.

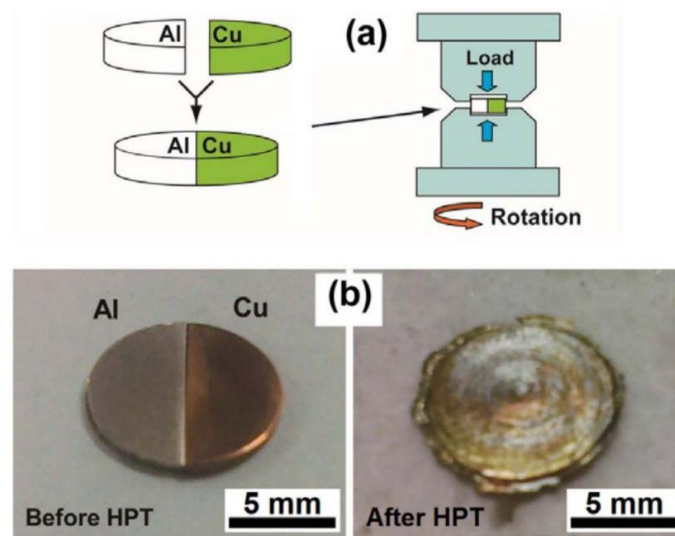


Figure 2.9 (a) Schematic of HPT processing of semicircle samples and (b) photos of Al-Cu sample before HPT and after HPT for 100 turns and 6 GPa [47]

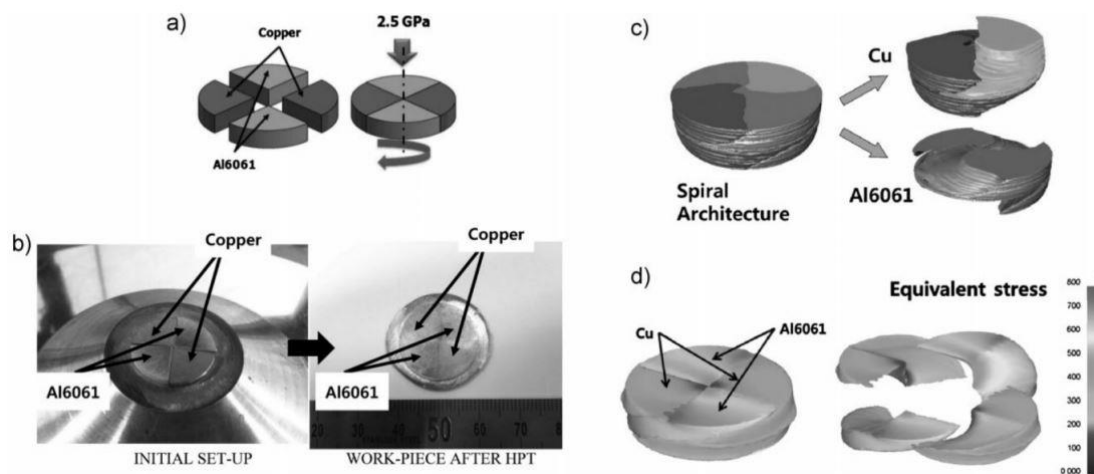


Figure 2.10 (a) Schematic of a quarter-circle Cu-Al6061 disk. (b) photos of quarter-circle Cu-Al6061 specimens prior to HPT test (left) and after a full turn of HPT anvil. (c) Computer model of the HPT-processed four-piece Cu-Al6061 specimen after a full turn of HPT anvil. (d) Computer model of von Mises stress after a half-turn of the HPT anvil [48]

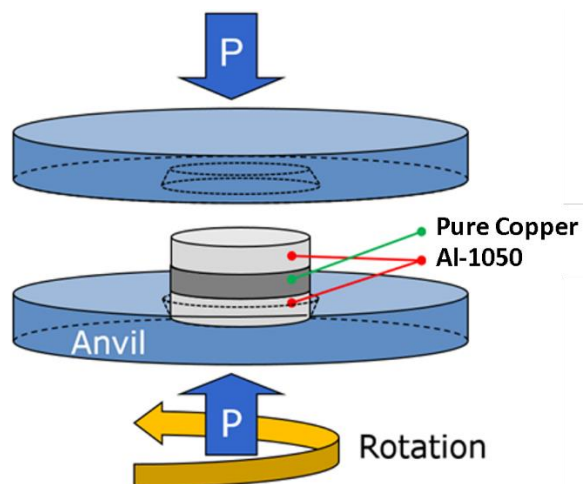


Figure 2.11 Schematic drawing of a mechanical bonding sample set-up in a quasi-constrained HPT condition [49].

3 Experimental Procedures

3.1 Material Processing

The materials used in these experiments were: a commercial purity aluminum Al-1050 alloy containing 0.4 wt.% Fe and 0.25 wt.% Si as major impurities with <0.07 wt.% Zn and <0.05 wt.% Cu and Mg as minor impurities, and a commercial purity copper alloy with 99.9 wt.% Cu. The alloys were extruded billets of approximately 10 mm diameter and cut into approximately 1 mm thickness disks with a silicon carbide saw blade. The Cu disks were annealed at 600 °C for 1h in a Lindberg/Blue induction heating oven. The disks were polished first with silicon carbide paper from Allied High Tech Products, Inc. of 200, 800, 2000 grit. The final thickness of the disks was approximately 0.83 mm. A MTDI MPE series polisher was used to polish the samples, under aqueous conditions with silicon carbide paper.

The samples were processed under quasi-constrained HPT condition as shown in Figure 2.4(c), with an aluminum disk on the top and bottom and a copper disk in the middle. Such sets of disks were placed in the depression of the lower anvil and aligned as shown in Figure 2.11. The HPT facility applied a pressure, P , of 6 GPa to the disks which caused the majority of the outflow of the material. Shear stress was applied at 1 full rotation per minute by the bottom anvil, N , for 10, 20, 30, 40, 50, 60 minutes. These experiments were conducted at room temperature, while the end temperature of the thermal couple inside the HPT rose to about 70 °C. Figure 3.1 shows a photograph of the HPT facility.



Figure 3.1 Photograph of HPT facility with anvils apart.

The processed samples were cut into semi circles along the disk diameters with a silicon carbide blade and fixed inside an acrylic mold to polish the cross-sectional areas. For further polishing of cross-sectional area, colloidal silica suspensions with particle sizes of 0.5 micron and 0.05 micron were used under ethanol conditions.

3.2 Characterization

Optical micrographs and the Vickers microhardness values were taken using a Mitutoyo HM-200 automatic hardness testing system on 20, 40, 60 rotations samples. A series of optical micrographs were taken for each specimen at a cross-section at a magnification of 100 \times and stitched together. Vickers microhardness was measured at a 150 gf load on a rectilinear grid pattern with a spacing of 0.16 mm. It is reasonable to note that the Vickers microhardness values of the separate base Al and Cu disks are ~20 and ~50, respectively.

The semi-circle surfaces were polished down to the mid-surfaces in the disk as shown in Figure 4.2 and X-ray diffraction patterns on the 20, 40 and 60 turn samples were taken. A Bruker-AXS D8 Discover was used to measure the X-ray scatter using a Cu K α source and a scanning speed of 1 $^\circ$ /min. Phase distributions were approximated using Materials Analysis Using Diffraction (MAUD) software [53], which used the Rietveld method for full pattern fitting. Micro-XRD methods were applied on the edge and center of the vertical cross-sections (as shown in in Figure 4.1) with an approximate accuracy of 1 mm².

SEM images were taken using a FEI Quanta 600F to detect flow and mixing of HPT processed samples. Compositional maps were obtained using energy dispersive spectroscopy (EDS) in a scanning SEM mode for the sample edge after 10 HPT revolutions. Detailed microstructural analysis was conducted by transmission electron microscopy (TEM) using a JEOL JEOM-2100F for the disk edges after 20 and 60 revolutions. The TEM specimens were taken at a distance of 1 mm from the edges of the processed disks and specimens were prepared using a focused ion beam, FEI Quanta 3D FEG. Compositional maps were also obtained using energy dispersive spectroscopy (EDS) in a scanning TEM mode.

3.3 Collaboration work - Nanoindentation

The novel technique of nanoindentation was conducted as a collaboration work at Hanyang University, South Korea, and the data analysis was performed at Oregon State University. A nanoindentation facility, Nanoindenter-XP (formerly MTS; now Keysight, Santa Rosa, CA) with a three-sided pyramidal Berkovich indenter having a centerline-to-face angle of 65.3° was used for the measurements. More than 15 indentations were conducted at the disk edges at each indentation strain rate to provide statistically valid data. All measurements were conducted under a predetermined maximum peak load of $P_{\max} = 50$ mN at constant indentation strain rates, $\dot{\epsilon}_i$ of 0.0125, 0.025, 0.05 and 0.1 s^{-1} .

4 Results

4.1 Microstructure: Overview

Figure 4.1 shows optical micrographs of the vertical cross-sections of the HPT processed disks under 6 GPa at room temperature after, from top to bottom, 1, 20, 40, 60 rotations. These samples were cut along the diameter, with the exposed vertical cross-section polished. The phase with bright color denotes the Al-rich phase, the dark regions correspond to the Cu-rich phase and the grey color at the disk edges relates to a mixture of Al and Cu.



Figure 4.1 Optical micrographs of vertical cross-sections of the HPT-processed Al-Cu disks from top to bottom: 1, 20, 40, and 60 rotations.

After 1 rotation by HPT, the Al and Cu alloys are bonded throughout the disk diameters and formed a layered structure. The interfacial boundaries are clear without any visible void and segregation. Additional rotation for up to 60 kept the consistent metal bonding of Al and Cu at the disk centers, while necking and bending of the phases are apparent by the wavy interfacial boundaries.

On the contrary, after 20 rotations, the copper phase near the edges fragmented into small phases within the Al matrix and formed a multi-layered microstructure at $r > 4.0$ mm. Increasing numbers of revolution through 40 by HPT demonstrated a mixture of very fine Cu phases within the Al matrix at the disk edge of $r > 2.0$ mm. Furthermore, additional HPT to 60 revolutions formed a wide peripheral region showing a complete mixture of Al and Cu at $r > 1.5$ mm.

In summary, the formed Al-Cu system demonstrates a reasonable radial sympathy in the deformed microstructure as well as significant microstructural heterogeneity along the disk diameter up to HPT for 60 rotations.

Figure 4.2 shows optical micrographs of the semi-circle Al-Cu disk surfaces which were polished down to approximately 1/3 of the thicknesses to visualize the phase distributions within the disks after, from top, 20, 40 and 60 rotations by HPT at 6 GPa at room temperature. As was mentioned for Figure 4.1, the different color in Figure 4.2 designate different phases and phase mixture. The sample surface after 20 rotations shows an absence of the Cu phase at the wide disk center due to the absence of the severe mixture of Al and Cu at the central region with less accumulation of strain as estimated by equations (2.2) and (2.3).

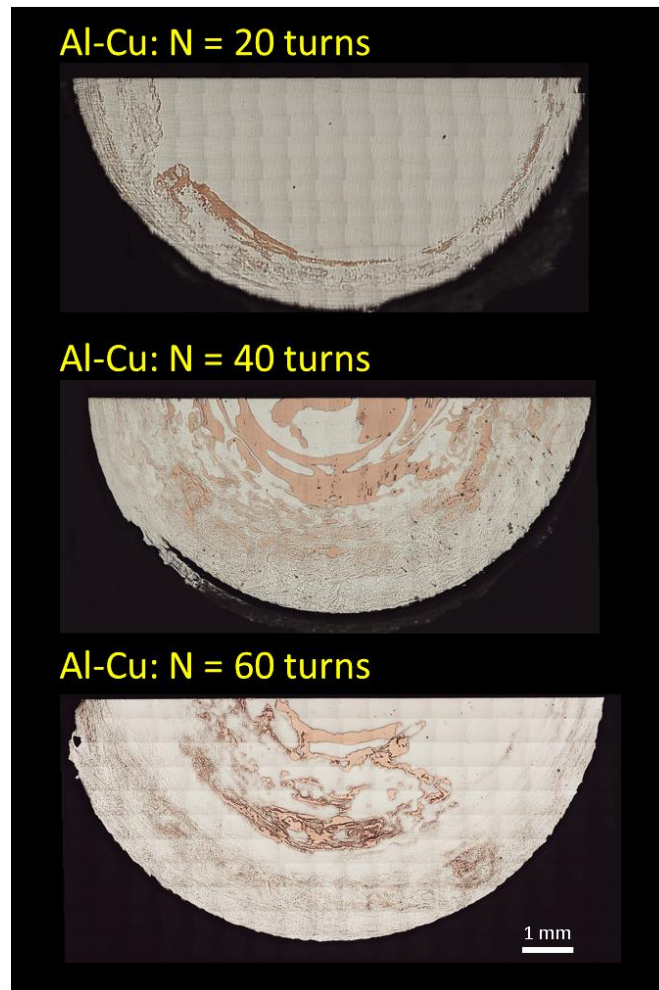


Figure 4.2 Optical micrographs taken on the surfaces near the mid-thickness of the HPT-processed Al-Cu disks from top to bottom: 20, 40 and 60 revolutions.

However, the disk surfaces after 40 and 60 rotations show a large Cu phase in a wide region at the disk centers at $r < 2.5\text{-}3.0$ mm towards the rest of the disk peripheries having fine Cu phases in the Al matrix and a severe mixture of these phases. This result affirms the results from the vertical-cross sections in Figure 4.1 that there is essential microstructural symmetry along the disk radial direction, but the phase mixture of Al and Cu is heterogeneous in the disk centers and edges.

4.2 Hardness along Disk Diameter

Figures 4.3 and 4.4 show the hardness profile along the diameter of the vertical cross-sections of the HPT-processed Al-Cu disks after 20, 40 and 60 rotations at 6 GPa and room temperature. Specifically, Figure 4.3 shows the hardness profile taken along the disk diameters at near-surface and mid-height (or mid-section) and the average of these hardness values for the Al-Cu disks after (a) 20, (b) 40 and (c) 60 rotations. There are two important findings from the hardness measurements.

Firstly, hardness increases significantly near the edges of all disks where fine Cu phases are distributed in the Al matrix, while hardness decreased dramatically towards the disk centers where the Al and Cu phases forms a simple layered microstructure. In practice, the disk edge after 20 HPT rotations shows the high hardness of <300 with some exceptions of ~ 400 , and the values increased to over 300 after 40 HPT rotations. Additional rotation to 60 further increased the hardness to ~ 420 at the disk edge. On the contrary, the central area remained the hardness consistent at ~ 130 up to $r \approx 4$ mm, 3.5 mm and 2 mm for the disks after 20, 40 and 60 revolutions, respectively. Such heterogeneous distribution of hardness with increasing numbers of HPT rotations are directly correlated with the heterogeneous microstructure observed in Figures 4.1 and 4.2.

Secondly, the difference in hardness taken at different sections are apparent at the disk peripheries for all disks after HPT, while the disk central regions demonstrate ignorable difference within the disk thickness. Specifically, the hardness taken at the mid-sections are lower than that at the surface planes for all HPT-processed disks after 20-60 rotations at $r > 3.0$ mm. This result confirms the hardness heterogeneity within the disk thickness in the diffusion-bonded Al-Cu system.

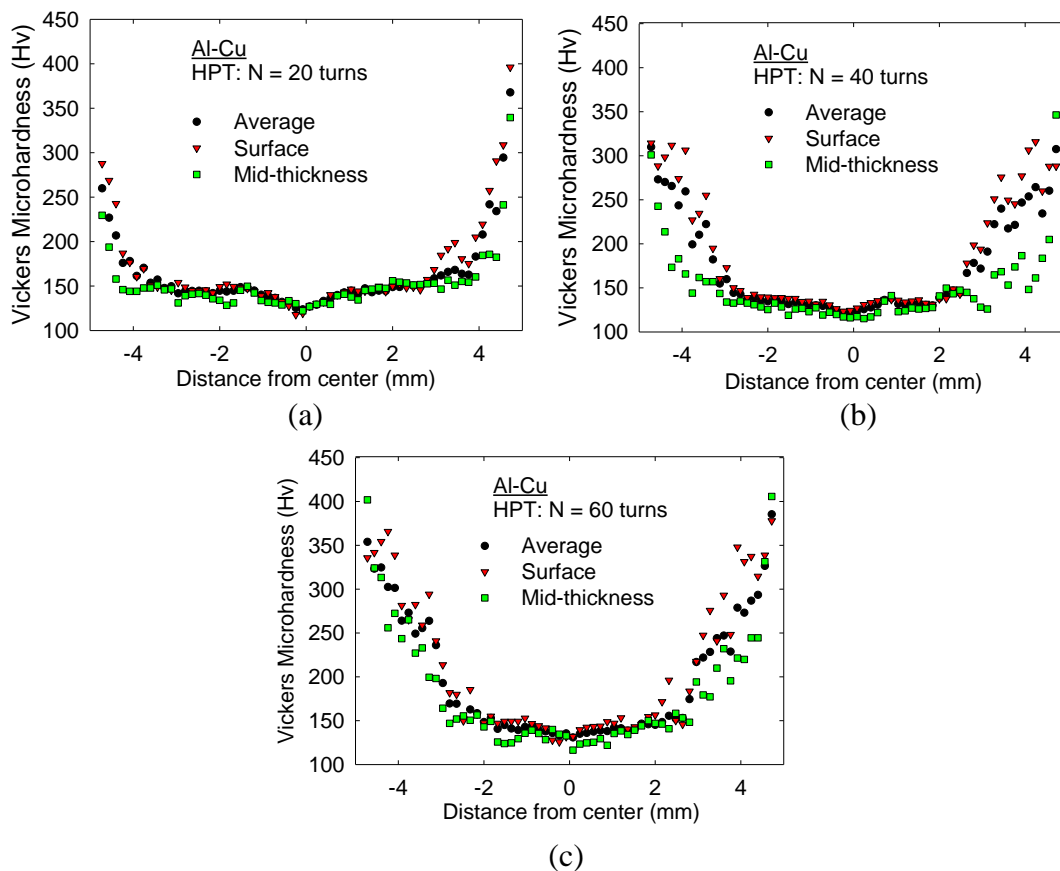


Figure 4.3 Vickers microhardness variations for the HPT-processed Al-Cu disks measured at near-surface and mid-height and the average of these on the vertical cross-sections after 20, 40 and 60 rotations at 6 GPa.

The hardness results in Figure 4.3 are replotted in Figure 4.4 to show the hardness evolution at (a) near-surfaces and (b) mid-sections in the disk height of the Al-Cu system after HPT for 20 and 60 turns. From both plots, it is apparent that disk peripheries with high hardness are expanded with increasing numbers of HPT rotations from 20 to 60. However, the trend of widening the disk peripheral region with high hardness is slightly less at the mid-sectional planes than the near-surfaces of the disks. In practice, the low hardness of ~ 130 at the disk center ends to have increased hardness at $r \approx 4.0$ mm after 20 HPT rotations and it shift to $r \approx 2.0$ mm after 60 rotations at the near surfaces of the Al-Cu disks. However, those hardness transition occurs at $r > 4.0$ mm and ~ 3.0 mm after 20 and 60 rotations at the mid-sections of the Al-Cu disks. These plots again visualize the occurrence of the hardness heterogeneity especially at the disk edges in the Al-Cu system.

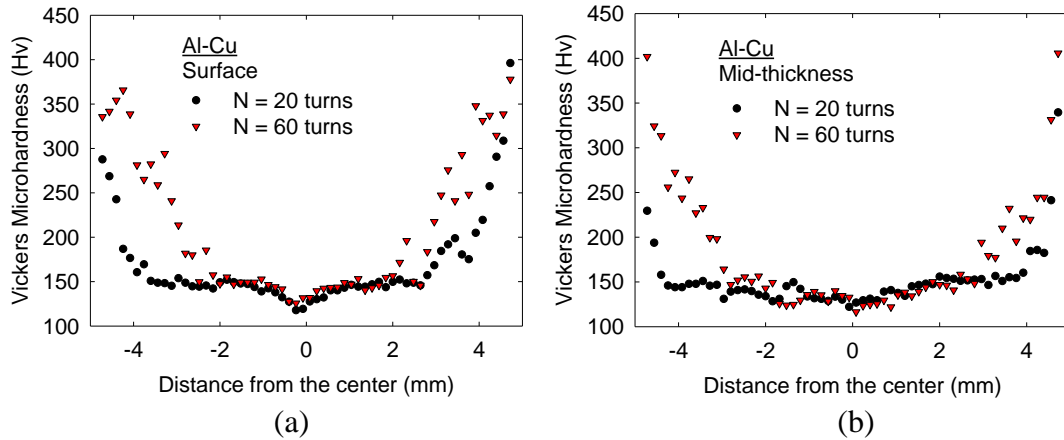


Figure 4.4 Comparison of the Vickers microhardness variations measured at (a) disk surfaces and (b) mid-sections for the HPT-processed Al-Cu disks after 20 and 60 rotations at 6 GPa.

Figure 4.5 shows color-coded hardness contour maps over the cross-sections of the Al-Cu disks after HPT for (from top) 20, 40 and 60 rotations at 6 GPa. The color key is shown in left of each map. As was shown in Figures 4.3 and 4.4, the hardness maps demonstrate the hardness increase at the disk edges, while the disk centers mid-section remains unchanged from 20 to 60 turns. But the expansion of the high hardness at the disk edges is clear with the exhibition of the hardness with these maps.

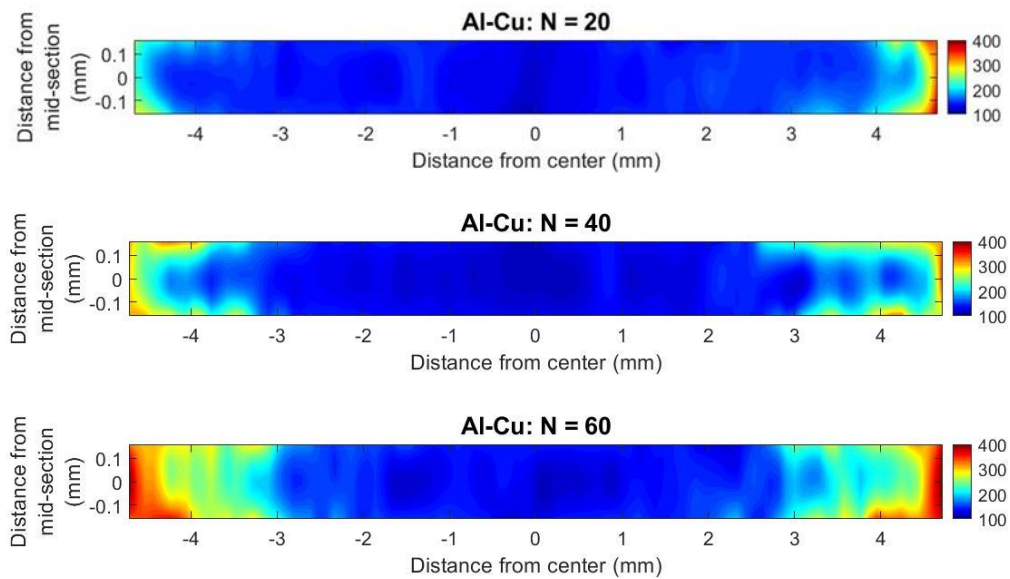


Figure 4.5 Contour plots of Vickers microhardness taken at the cross-sections of the HPT-processed Al-Cu disks after 20, 40 and 60 turns at 6 GPa.

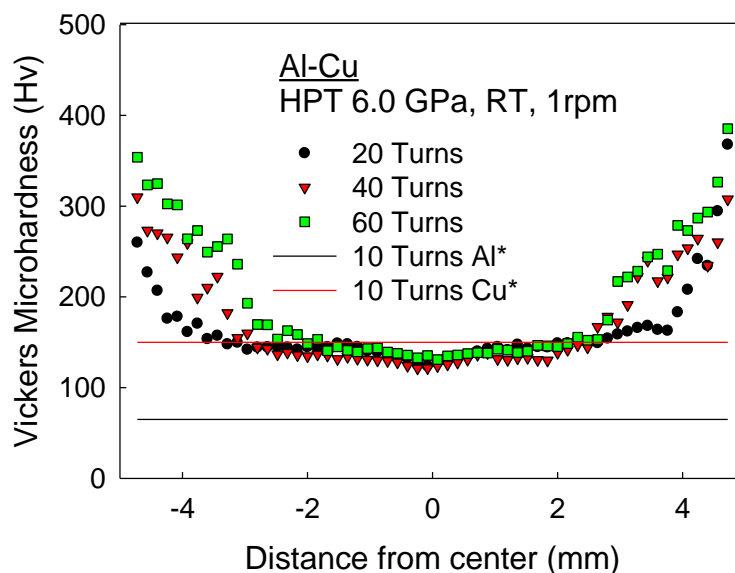


Figure 4.6 Variation of Vickers microhardness for the HPT-processed Al-Cu disks measured from the vertical cross-section after 20, and 60 turns at 1 rpm, room temperature and 6 GPa. For comparison purposes, high purity Al [54] and Cu [55] after 10 HPT rotations are inserted in the plot.

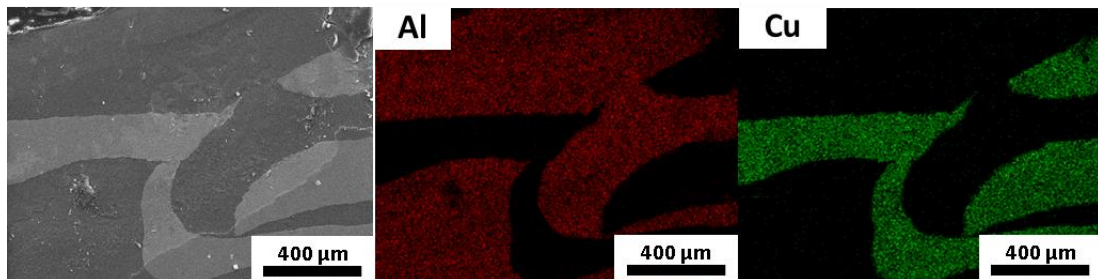
Evolution of hardness with increasing numbers of HPT evolution is shown in Figure 4.6 where the hardness values for each disk are taken from the mean values shown in Figure 4.3. For comparison purposes, high purity Al [54] and Cu [55] after 10 HPT rotations are inserted as black and red lines, respectively, in the plot. The selection of 10 turns is due to the saturation in grain refinement, thus hardness and other mechanical properties, when these simple metals are processed by HPT separately for more than 5 turns at 6 GPa or higher [56]. Thus, the hardness values of high purity Al after HPT processing saturates at ~ 65 after 10 revolutions, while high purity Cu saturates at about ~ 150 Hv [55].

It should be noted that after 20 or higher HPT rotations the disk central regions showing lower hardness has at least the minimum hardness of ~ 130 - 150 Hv which is higher than the base material of Al can achieve and similar to the hardness Cu can achieve. The plot demonstrate shows an apparent enhancement in hardness at the disk peripheries with increasing numbers of HPT rotations. These improved hardness values are not achievable when the base materials of Al and Cu are processed separately. Thus, there is a feasibility of improving hardness by mechanical bonding of the separate metals by the HPT process.

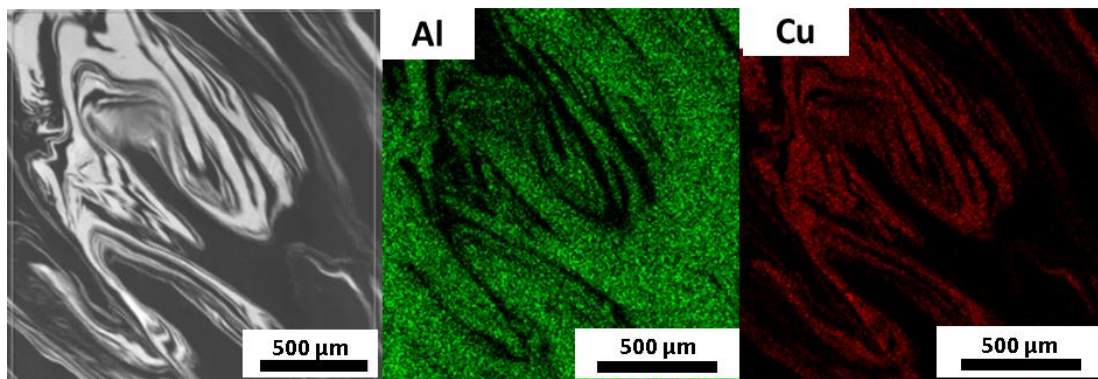
4.3 Elemental Analysis

Figure 4.7 shows scanning electron microscope images as well as energy dispersive x-ray analysis after (a) 10, (b) 20 and (c) 60 turns near the edge of the disk. In the SEM images (left most image in each group) the light grey area shows high amounts of copper while the dark grey areas show high amounts of aluminum.

(a) Al-Cu: $N = 10$ turns



(b) Al-Cu: $N = 20$ turns



(c) Al-Cu: $N = 60$ turns

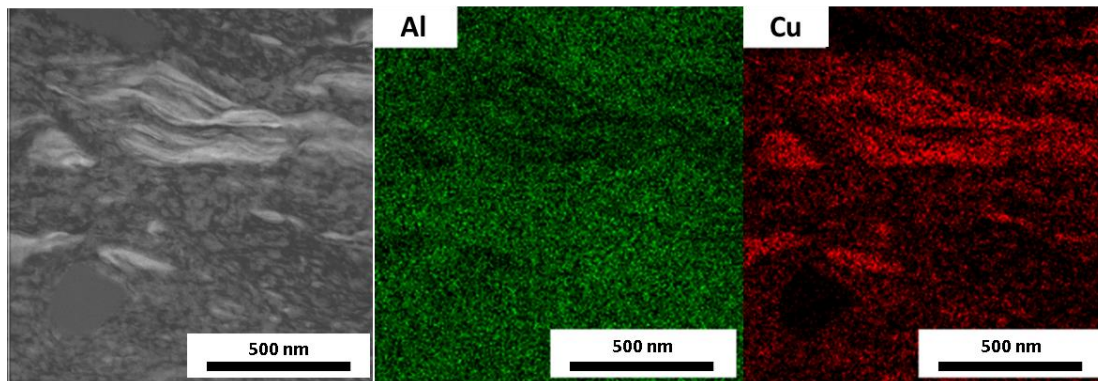


Figure 4.7 SEM and EDX images taken at the disk edges of the Al-Cu HPT samples after (a) 10, (b) 20 and (c) 60 turns.

The EDX images in the second column and third column show the concentration of aluminum and copper atoms colored with red and green. After 10 anvil rotations, the Al and Cu phases have clear, well-defined borders indicating the separate phases are not well mixed. After 20 turns, thinner phases of Al and Cu in between each other shows increased flow and mixing by HPT. After 60 turns the border between the phases are difficult to determine and EDX images show that at a nano-scale, Al and Cu atoms are more evenly distributed. This suggests that the Al and Cu phases are well mixed, and microstructure refined severely at the edge. Severe refinement of microstructure may be an influence on hardness increase and phase evolution.

4.4 X-ray Diffraction

Figure 4.8 shows X-ray diffraction patterns of Al-Cu HPT samples after 20 and 60 turns on the mid-thickness and Table 4.1 show the Maud quantitative analysis on the XRD patterns of Figure 4.8. Notable Al_2Cu peaks show after 60 turns, suggesting formation of intermetallic phases from increased processing by HPT. Large Al peaks show abundance of Al in both samples. Table 4.1 shows over 90% Al phase after 20 turns coincide with the microstructure overview image in Figure 4.2 that most of this sample surface was covered by Al after mid-thickness polishing. Figure 4.8 shows peak broadening, especially Cu and Al peaks in 2θ between 40 and 50 degrees. This peak broadening could be caused by lattice distortions formed by increased HPT processing turns.

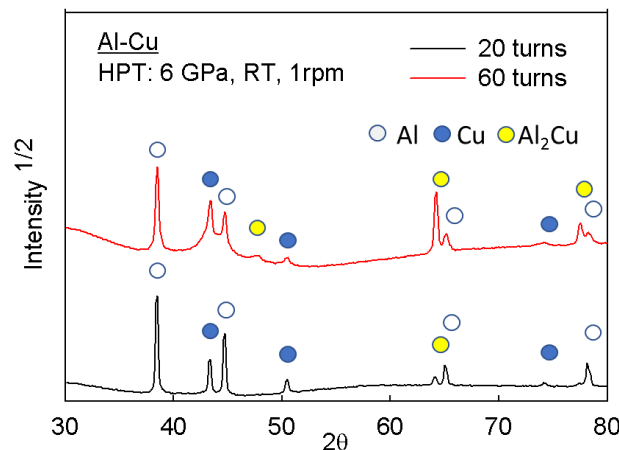


Figure 4.8 X-ray diffraction profiles for the Al-Cu HPT samples after 20 and 60 turns.

Table 4.1 Summary of the phase fractions result though MAUD on XRD profiles as Figure 4.8

	20 turns	60 turns
Al	90.93% \pm 6.76	31.53% \pm 6.9
Cu	4.17% \pm 0.61	14.92% \pm 5.5
Al₂Cu	4.89% \pm 1.40	53.54% \pm 9.1

Figure 4.9 and Table 4.2 show the XRD profiles and MAUD quantitative analysis, respectively, taken at the edge and center of a vertical cross-section of the Al-Cu HPT sample after 60 turns. The increase background noise comes from the low relative intensities of the peaks from a 1 mm² X-ray beam. Small amounts of peak broadening visible from the edge XRD pattern suggest more lattice distortions near the edge than the center. This is also predicted from equation 2.3 where equivalent strain increases as the radius increases. Table 4.2 shows relatively consistent Al content, while showing a slightly increasing Al₂Cu intermetallic phase at the edge. These XRD analysis suggest that the Al₂Cu intermetallic phase is correlated to the hardness measured after HPT processing. Only the most common intermetallic phase

of Al_2Cu was applied to these analyses maintain simplistic assumptions for the MAUD quantitative analysis software and keep error at a minimum.

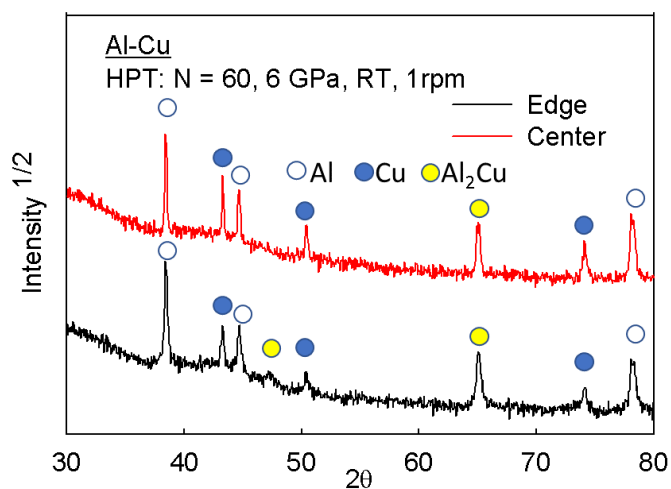


Figure 4.9 Micro-X-ray diffraction patterns taken at the disk edge and center for the Al-Cu HPT samples after 60 turns. Beam size 1 mm^2 .

Table 4.2 Summary of the phase fractions result though MAUD on XRD profiles as shown in Figure 4.9

	Center	Edge
Al	33.72% \pm 7.3	30.59% \pm 9.2
Cu	12.44% \pm 4.1	2.08% \pm 2.4
Al_2Cu	54.55% \pm 4.7	67.91% \pm 4.7

4.5 Nanoindentation

Figures 4.10 and 4.11 show the load-displacement curves acquired through the nanoindentation measurements at strain rates of (a) $1.25 \times 10^{-4} \text{ s}^{-1}$, (b) $2.5 \times 10^{-4} \text{ s}^{-1}$ (c) $5.0 \times 10^{-4} \text{ s}^{-1}$ and (d) $1.0 \times 10^{-3} \text{ s}^{-1}$ taken near the disk edges of the Al-Cu disks after 20 and 60 rotations, respectively. For all testing conditions, fifteen separate indentations are conducted for acquiring static data in this study.

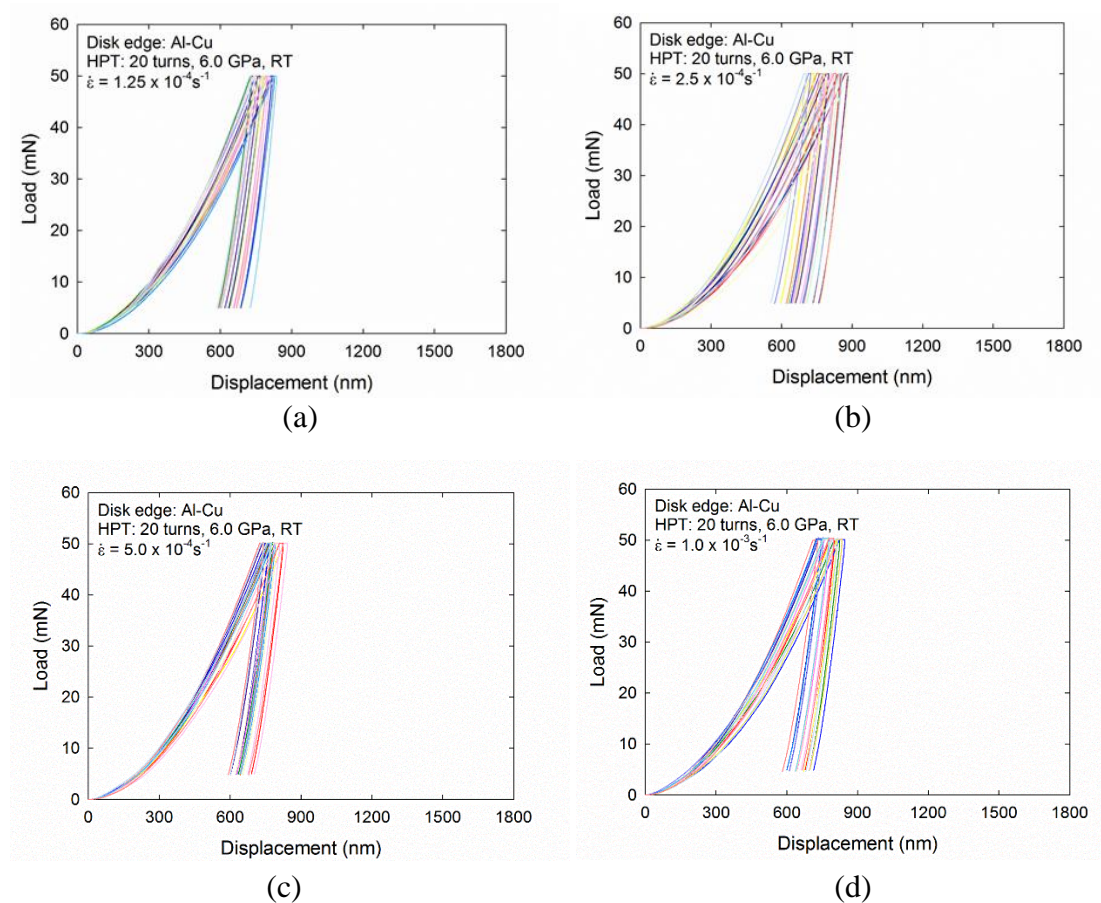


Figure 4.10 Load-displacement curves taken through nanoindentation at strain rates of (a) $1.25 \times 10^{-4} \text{ s}^{-1}$, (b) $2.5 \times 10^{-4} \text{ s}^{-1}$, (c) $5.0 \times 10^{-4} \text{ s}^{-1}$ and (d) $1.0 \times 10^{-3} \text{ s}^{-1}$ at the disk edges of the Al-Cu samples after 20 turns.

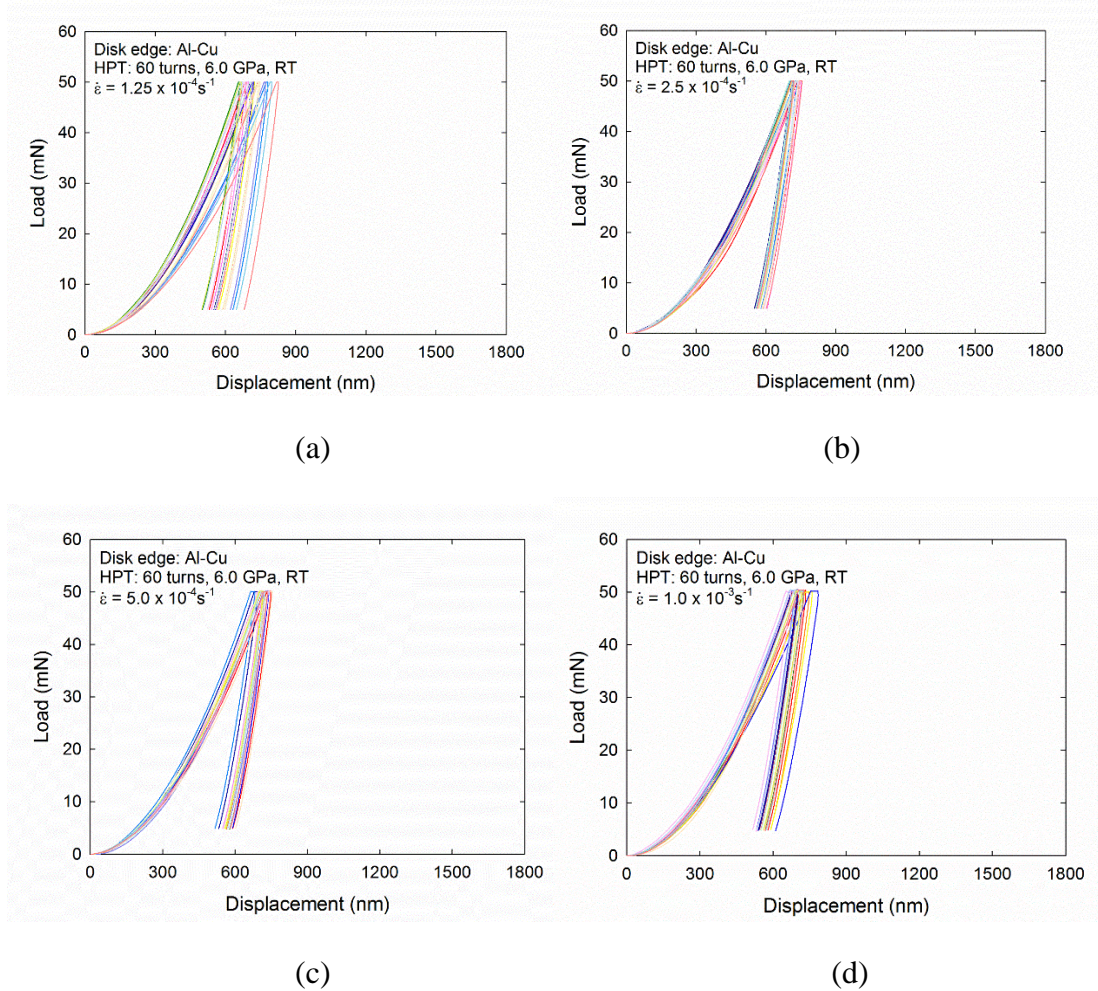


Figure 4.11 Load-displacement curves taken through nanoindentation at strain rates of (a) $1.25 \times 10^{-4} \text{ s}^{-1}$, (b) $2.5 \times 10^{-4} \text{ s}^{-1}$, (c) $5.0 \times 10^{-4} \text{ s}^{-1}$ and (d) $1.0 \times 10^{-3} \text{ s}^{-1}$ at the disk edges of the Al-Cu samples after 60 turns.

A series of the curves show larger deviations in micro-mechanical responses for all fifteen measurements at each strain rate, thereby indicating the plastic instability at the Al-Cu disk edge after 20 HPT turns. With increasing numbers of HPT turns to 60, the disk edge tends to show more consistent micro-mechanical responses. Moreover, the load-displacement curves confirm increased hardness at the disk edges after 60 HPT turns as the maximum displacements are reduced compared to 20 turns at all strain rates. A closer inspection shows the fifteen measurements tend to be closer with decreasing strain rate, though showing better plastic stability at slow strain rates in the Al-Cu system for both 20 and 60 HPT turns. It may be due to the

gradual phase mixture which may demonstrate the plastic instability when torsional strain is not high enough but further straining by increasing numbers of turns leads to consistent mechanical response. Moreover, detailed analysis shows a slight decrease in displacement as strain rates increase, thus the alloy system tends to demonstrate strain rate sensitivity in both alloy processing conditions.

5 Discussion

5.1 Significant Strengthening by HPT

The significant improvement in hardness in the Al-Cu system by processing through HPT may involve multiple strengthening mechanisms including grain refinement, solid solution strengthening, and precipitation hardening [56]. Grain refinement increases strength by an intensive increase of dislocation density which inhibit plastic deformation. An earlier study showed significant grain refinement down to an average grain size of 30 nanometers in the mechanically bonded Al-Cu alloy [57], which categorizes these materials as bulk nanostructured materials. Solid solutionizing generally occurs when dilute alloys having two-phase are heat treated and the separate phases start dissolving into one another, within solubility levels. These solute atoms disrupt the regular crystal lattice they are in would delay the dislocation movements leading to solid solution strengthening of the material. In the present material of the Al-Cu system, although the processing was conducted at room temperature, high pressure processing accelerates the diffusion of both Al and Cu atoms as seem in Figure 4.7, thereby a limited contribution of solid solution strengthening within the Al matrix is anticipated. Precipitation hardening occurs when a second phase precipitates out at a sufficiently high concentration of solute which acts as another, larger barrier to dislocation movement. In the present case, an intermetallic compound of Al_2Cu were nucleated during the mechanical bonding of Al and Cu for high HPT turns and the precipitates contribute to the exceptional hardness of the synthesized Al-Cu alloy system. These three strengthening mechanisms are concurrently activated by the increased strain and high compressive pressure to the Al-Cu system material during HPT [49].

Using equation 2.3 to calculate equivalent strain based on the locations of the hardness measurements, a plot of hardness versus equivalent strain was constructed and is it shown in Figure 5.1 where the measured Vickers microhardness values against to the calculated equivalent strain are plotted at various distances across the disk radius for the Al-Cu disks processed for $N = 20, 40,$ and 60 turns. The applied Vickers microhardness values are averages of those taken at disk surfaces.

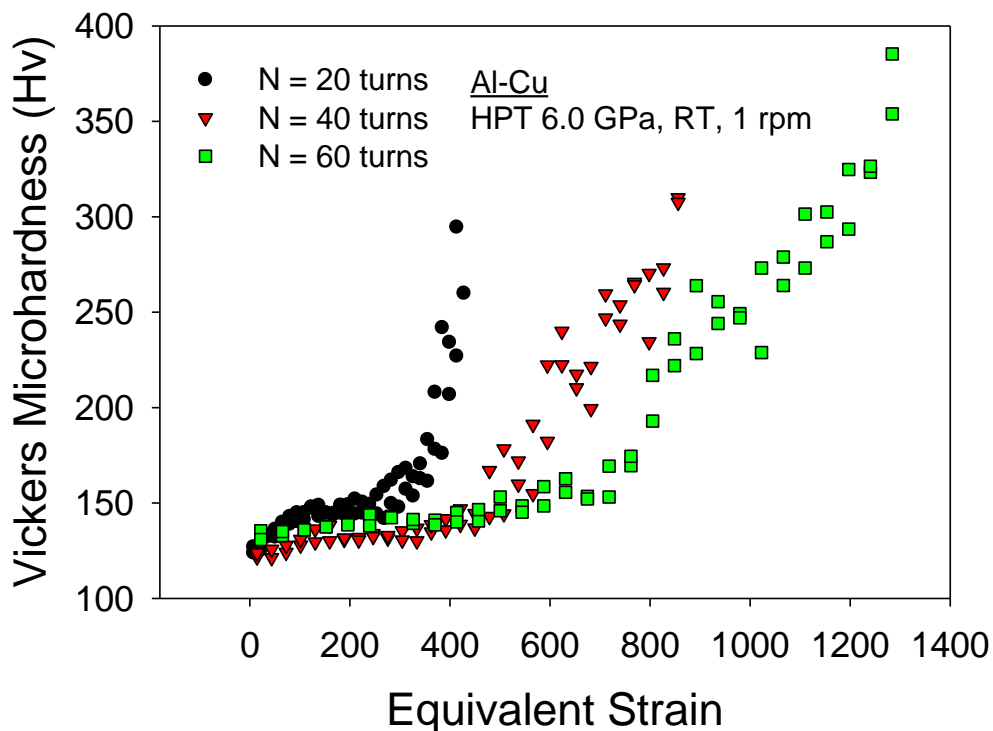


Figure 5.1 Vickers Microhardness vs Equivalent Strain for $N = 20, 40$ and 60 turns Al-Cu HPT processed disk. Equivalent strain was calculated with equation 2.3

Figure 5.1 suggests an exponential increase in hardness with increasing torsional strain for all disks up to 60 HPT turns. Moreover, with increasing total numbers of HPT turns, the maximum achievable hardness increases without any saturation for the Al-Cu alloy system under the current processing conditions. It is apparent with $Hv = 396$ after 60 turns in comparison with $Hv = 302$ after 20 turns. However, with increasing the HPT turns, higher values of equivalent strain are required to obtain a specific high hardness value. For instance, $Hv = 300$ can be achieved with equivalent strain of 300 in the Al-Cu disk after 20 HPT turns, while equivalent strains of ~ 850 and ~ 1200 is required for the disks after 40 and 60 turns. This may be due to the inevitable heat generation during HPT that is attributed to the friction between the anvils and the disk sample. From the thermo-couple placed very close to the sample contacting location in the HPT anvil, a temperature rise can be measured during the mechanical bonding through HPT. In practice, the processing temperature slowly increased from room temperature up to $70\text{ }^{\circ}\text{C}$ in the first 15-20

minutes including the compression stage to the following anvil rotation for up to 20 turns and it remained constant duration of the rest of processing. The generated heat causes microstructural recovery of the introduced ultrafine grains and competes with the applied strain in the grain refinement process. This may explain the required higher values of equivalent strain to achieve similar levels of hardness with increasing numbers of HPT turns.

It is reasonable to note that there are three different models of hardness behaviors with increasing equivalent strain for ultrafine-grained materials [58] as shown in Figure 5.2 where these schematic plots gives the changes in hardness with increasing values of equivalent strain by HPT as computed by using equation 2.3.

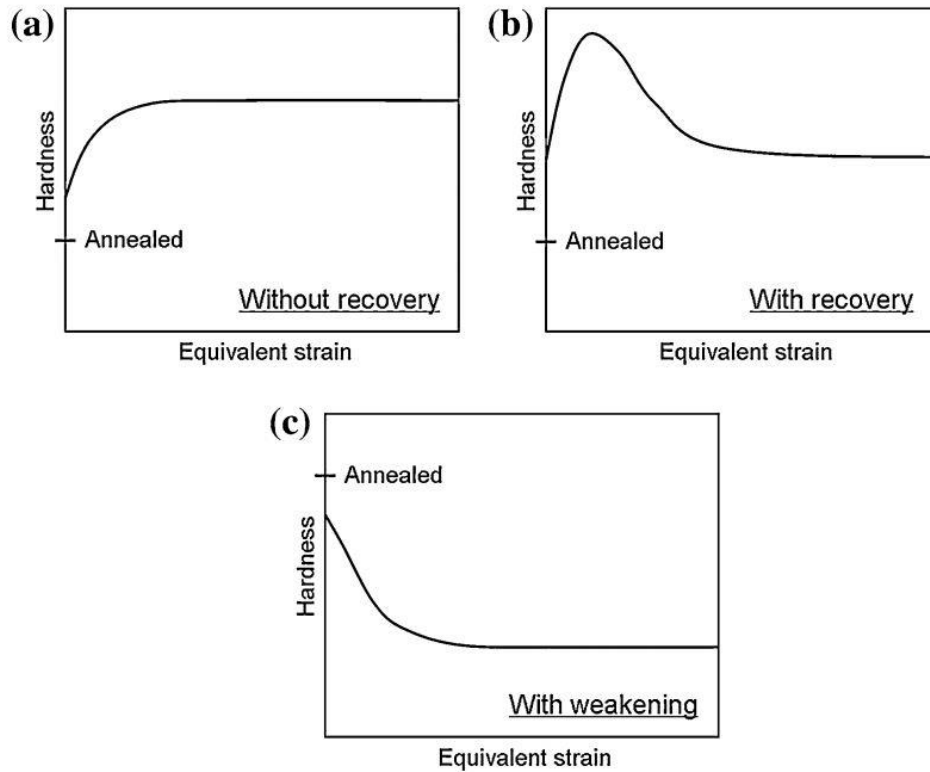


Figure 5.2 Schematic illustration of three models of variation of hardness with equivalent strain for metals processed by HPT: a) hardening without recovery, b) softening with rapid recovery, and c) weakening: typical levels for the initial annealed conditions are also indicated [58]

It was defined that these three different behaviors appears depending on the melting temperature, T_m , of the material. Specifically, the computed homologous temperature of processing (T/T_m) where the processing temperature is room temperature for HPT is low, the material shows the most common hardness behavior of hardening without recovery as shown in Figure 5.2(a) and most commercial purity metals and alloys behave the hardness model. The other two models of softening with recovery in Figure 5.2(b) and weakening without peak hardness in Figure 5.2 (c) are demonstrated by high-purity metals and the materials having low T_m , respectively.

In the present study, the base metals of both Al-1050 and commercial purity Cu demonstrate a behavior of hardening without recover as schematically shown in Figure 5.2(a). Thus, these base metals show saturations in an increasing of hardness after grain refinement as the saturated high hardness are shown in Figure 4.6. On the contrary, the mechanically bonded Al-Cu shows an exponential hardness increase with increasing equivalent strain without any hardness saturation in the present processing conditions. Therefore, the mechanical bonding by means of HPT processing shows a considerable potential for the synthesis of unique alloy systems which can have high hardness without any upper limit with applying further straining.

5.2 Homogeneity in Hardness

The contour plots in Figure 4.5 show the hardness distributions on the vertical cross-sections of the mechanically bonded Al-Cu alloy. There is a significant hardness gradations along the disk radius which are anticipated by the variation in applied strain within a disk as given by equation 2.3. This hardness gradations along the disk radius have been homogenized in previous work in pure alloys where sufficient torsional strain (number of turns) has been applied to process the HPT disks [54,55]. However, for the harder hybrid Al-Cu system, the hardness homogenization process tends to require more torsional strain than in the current processing conditions.

In contrast to the disk radial directions, significant homogeneity was observed in the disk thickness direction, specifically near the disk center where the Al and Cu layers look separated in Figure 4.1. Some microhardness indentations were conducted within the Cu layer near the mid-thickness of the disks and some others are at the Al layer near the surfaces. However, the hardness taken from both layers of dissimilar metals show around 150 Hv. This hardness value is similar to the HPT-processed Cu disks after 10 turns showing the saturation of hardness [55], but it is much higher than the HPT-processed Al disks after 10 turns showing the saturated hardness of 65 Hv [54]. This is likely due to the influence of the interfaces as well as a limited contribution of solid solution hardening. Following the measurement standards, the microhardness indentations were spaced apart over four times the max indentation size, however they may not have been sufficiently spaced from the Al-Cu interfaces. This may cause the strengthening of the thin layers of both Cu and Al adjacent to the interfaces. It is also possible that trace amounts of Cu diffuse into the Al matrix near the center of the disk under high pressure such that there is a hardening through solid solution. EDX analysis near the edge shows little mixing at low strain, but there is weak signal of Cu dissolved in Al after 20 turns in Figure 4.7. This strong interface effect shows good mechanical bonding and suggests the mechanical bonding by HPT of dissimilar metal disks is potentially an excellent method of utilizing diffusion bonding to introduce hybrid alloys.

5.3 Specific Strength

Taking advantage of bonding of lightweight Al with Cu, there is a potential of increasing specific strength in the mechanically bonded alloys. Thus, in this section, specific strength is calculated by measuring the density of the severely deformed Al-Cu disk edges and taking the measured Vickers microhardness to estimate the yield strength. Often strength is correlated with hardness by a factor C , as show in equation 5.1:

$$\sigma = \frac{Hv}{C} \quad (5.1)$$

where the constant C depends on the stages of deformation, such as elastic, elastic-plastic and fully plastic, and the Vickers microhardness measurement can provide fully plastic deformation which provides the value of $C = 3$. σ is the tensile strength and Hv is the Vickers microhardness. Previous work on HPT has shown C to be around 3.3 for these types of processed materials [60].

Thus, equation 5.1 is used for estimating the tensile strength of the mechanically bonded Al-Cu alloy after HPT for 20 and 60 turns and subsequently the specific strength. For references, the estimation was conducted for the base metals of Al and Cu with using their saturated hardness after grain refinement by HPT.

Table 5.1 (Columns 2-5) Density of the material, maximum hardness measured at the edge for hybrid materials, estimated tensile strength, specific strength.

**Maximum hardness for the 20-turn sample was the average of both edge measurements as one edge was significantly harder than the other due to misalignment of the HPT anvils.*

***Estimated tensile strength was computed using equation 5.1.*

	Density (g cm⁻³)	Maximum Hardness (Hv)	Tensile Strength** (MPa)	Specific Strength (MPa cm³ g⁻¹)
Al-Cu 20 turns	4.466 ^[58]	346*	1142	255.7
Al-Cu 60 turns	4.321 ^[58]	407	1343	310.8
Al 10 turns	2.73 ^[60]	65 ^[60]	215	80 ^[60]
Cu 10 turns	8.96 ^[60]	150 ^[60]	495	55 ^[60]

Table 5.1 shows a summary of the measured density and hardness, estimated tensile strength and the estimated specific strength of the Al-Cu alloys. It is apparent that the densities of the hybrid alloy system are lowered and the hardness and thus strength are improved, thereby improving specific strength of the Al-Cu alloy after the mechanical bonding. The specific strength is further improved by increasing numbers of HPT turns due to the lowered density with improved hardness. It is interesting to note that the base metals of Al and Cu processed by HPT have comparable tensile strength and specific strength with 304 steel (505 MPa tensile strength and $63.1 \text{ MPa cm}^3 \text{ g}^{-1}$ specific strength [60]). The Al-Cu hybrid system shows a significant improvement of mechanical properties including tensile strength up to 1343 MPa and specific strength up to $310.8 \text{ MPa cm}^3 \text{ g}^{-1}$ after 60 turns and it surpasses the Titanium Beta C alloy (1250 MPa tensile strength and $260 \text{ MPa cm}^3 \text{ g}^{-1}$ specific strength [61]). In concluding, the mechanical bonding by HPT processing introduce new hybrid alloys from two separate conventional metals and the hybrid metal systems enable to demonstrate superior mechanical properties including exceptional specific strength.

5.4 Strain rate sensitivity

A series of load-displacement data sets taken by nanoindentation were analyzed to provide an important mechanical property of plasticity by computing the strain rate sensitivity values, m , for the disk edges in the mechanically-bonded Al-Cu system for 20 and 60 HPT turns. The value of m can be determined from the slope of the line in a logarithmic plot of $H/3$ against strain rate, $\dot{\epsilon}$, where H is the measured nanoindentation hardness. The estimated values of m for the Al-Cu disks in the plot are shown in Figure 5.3 for the disk edges of the hybrid alloy system. For comparison purposes, the base materials of Al and Cu after HPT for 10 turns and their m values are also included in Figure 5.3.

The strain rate sensitivity of $m \approx 0.03$ was estimated at the disk edge of the Al-Cu system after 20 HPT turns, but it may be even lower by considering the wider error bars arising from the plastic instability due to not enough phase mixture. Nevertheless, the m value after 20 HPT turns is between the values of 0.02 and 0.04 of the base metals of Al and Cu after HPT for 10 turns, respectively. Processing by HPT for 60 turns increased the m value to ~ 0.08 with reasonable plastic stability in the Al-Cu alloy. The m value is significantly higher than the base metals and increasing numbers of HPT turns on the hybrid system provides a significant enhancement in the m value, thereby demonstrating a potential for achieving improved plasticity in the processed materials.

Considering the results obtained in the study, the observed excellent plastic responses at the disk edges of the Al-Cu hybrid alloy processed by HPT lead to the conclusion that the mechanical bonding under concurrent grain refinement through HPT is an excellent processing strategy for fabricating lightweight UFG hybrid alloy systems having excellent mechanical properties and this approach can be applied to synthesize a wide variety of new engineering nanomaterials.

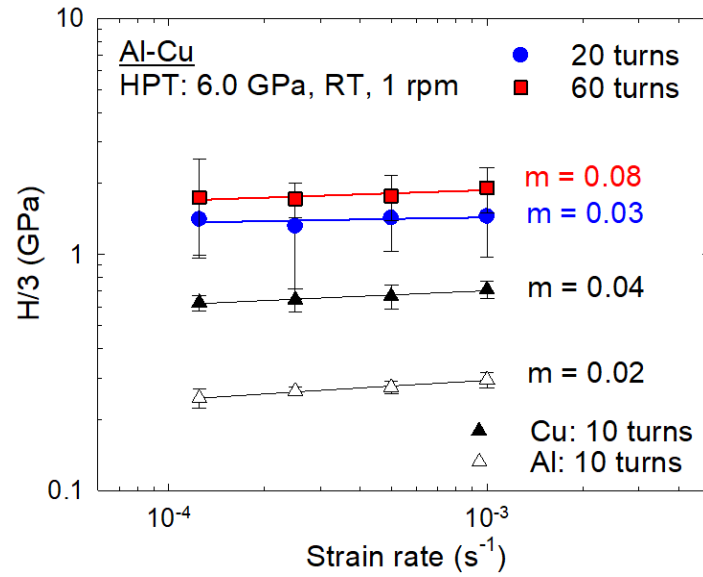


Figure 5.3 Estimated stress vs strain rate for nano-indentations of Al-Cu HPT processed disks near disk edge, 6 GPa, RT, for 20 and 60 turns. For references, the data for the base metals of Al and Cu are included. The strain rate sensitivity (m) values are estimated from the slopes of the lines.

6 Summary and Conclusion

- a) Aluminum and Copper commercial alloys were mechanically bonded by HPT at 6.0 GPa up to 60 turns at room temperature. The microstructure was refined and the dissimilar phases are severely mixed during processing. The hardness, phase composition and microstructure evolution was characterized.
- b) Significant improvements in hardness was observed up to 400 Hv at the disk edges of the mechanically bonded Al-Cu system after 60 turns. It is anticipated by the nucleation of an intermetallic compound of Al_2Cu during the mechanical bonding process.
- c) Homogeneity in hardness at the disk centers along the disk thickness direction is anticipated by the interfaces and a small contribution of solid solution strengthening. Hardness homogeneity was not achieved in the radial direction.
- d) The hardness behavior of exponential increase without hardness saturation was observed for the mechanically bonded Al-Cu system with increasing equivalent strain. This behavior is different from the base materials which shows the upper limit of hardness after grain refinement.
- e) Specific strength of $310.8 \text{ MPa cm}^3 \text{ g}^{-1}$ was observed at the disk edge of the Al-Cu hybrid system processed by HPT after 60 turns. This value is extremely competitive with high end alloys such as Titanium Beta C. The mechanical bonding of lightweight metals by HPT likely to produce exceptionally strong materials with lowering density.
- f) The Al-Cu system showed the improved strain rate sensitivity of 0.03 and 0.08 after HPT for 20 and 60 turns, respectively, thereby exhibiting the excellent plasticity of the hybrid alloy system.
- g) Processing by HPT of dissimilar metals demonstrated an excellent potential to develop a wide variety of new hybrid alloy systems having excellent mechanical properties.

7 Future Work

- a) The Cu-Al-Cu sandwich would be an interesting candidate for hybrid HPT processing as having the hard surfaces.
- b) Scaling up of the sample size would be important for the feasibility of mechanical bonding by HPT.
- c) Electric resistivity will be measured at 5 different locations across the disk radius to characterize the electrical properties of the mechanically bonded Al-Cu system. (Collaboration work with a group at Indian Institute of Science, Bangalore)
- d) A near term commercial manufacturing process would be tested by using the HPT rolling die set-up (installed in summer 2019) to continuously process Al/Cu thin plates to produce stronger conductive plates.

Bibliography

1. M. A. Meyers, A. Mishra, D. J. Benson, *Prog. Mater. Sci.* 51 (2006) 427-556
2. R. Z. Valiev, R. K. Islamgaliev, I. V. Alexandrov, *Prog. Mater. Sci.* 45 (2000) 103-189
3. R. Z. Valiev, Y. Estrin, Z. Horita, T. G. Langdon, M. J. Zehetbauer, Y. T. Zhu, *JOM* 58 (4) (2000) 33-39
4. E. O. Hall *Proc. Phys. Soc. B* 64 (1951) 747-753
5. N. J. Petch *J. of the Iron and Steel Inst.* 173 (1953) 25-28
6. T. G. Langdon, *Mater. Sci. Eng. A* 174 (1994) 225-230
7. T. G. Langdon, *Metall. Trans. A* 13 (1982) 689-701
8. M. Kawasaki, T. G. Langdon, *J. Mater. Sci.* 51 (2016) 19-32
9. R. Z. Valiev, I. V. Alexandrov, Y. T. Zhu, T. C. Lowe, *J. Mater. Res.* 17 (2002) 5-8
10. R. Z. Valiev, *Nature* 419 (2002) 887-889
11. R. Z. Valiev, *Nature Mater.* 3 (2004) 511-516
12. R. Z. Valiev, T. G. Langdon, *Prog. Mater. Sci.* 51 (2006) 881-981
13. A. P. Zhilyaev T. G. Langdon, *Prog. Mater. Sci.* 53 (2008) 893-979
14. E. Ma, *Src. Mater.* 49 (2003) 663-668
15. S. V. Divinski, J. Ribbe, D. Baither, G. Schmitz, G. Reglitz, H. Rösner, K. Sato, Y. Estrin, G. Wilde, *Acta Mater.* 57 (2009) 5706-5717
16. S. V. Divinski, G. Reglitz, H. Rösner, Y. Estrin, G. Wilde, *Acta Mater.* 59 (2011) 1974-1985
17. R. Z. Valiev, Y. Estrin, Z. Horita, T. G. Langdon, M. J. Zehetbauer, Y. T. Zhu, *JOM* 68 (4) (2016) 1216-1226
18. R. Z. Valiev, Y. Estrin, Z. Horita, T. G. Langdon, M. J. Zehetbauer, Y. T. Zhu, *Mater. Res. Lett.* 4 (2016) 1-21
19. R. Z. Valiev, R. K. Islamgaliev, I. V. Alexandrov, *Prog. Mater. Sci.* 45 (2000) 103-189
20. M. Furukawa, Y. Iwahashi, Z. Horita, M. Nemoto, T.G. Langdon, *Mater. Sci. Eng. A* 257 (1998) 328-332
21. M. Kawasaki, T.G. Langdon, *Mater. Sci. Eng. A* 503 (2009) 48-51

22. A. P. Zhilyaev, T. R. McNelley, T. G. Langdon, *J. Mater. Sci.* 42 (2007) 1517-1528
23. P. Kumar, M. Kawasaki, T. G. Langdon, *J. Mater. Sci.* 51 (2016) 7-18
24. T. Mungole, P. Kumar, M. Kawasaki, T.G. Langdon, *J. Mater. Sci.* 50 (2015) 3549-3561
25. P.W. Bridgman, *J. Appl. Phys.* 14 (1943) 273-283
26. K. Edalati, Z. Horita, *Mater. Sci. Eng. A* 652 (2016) 325-352
27. T. G. Langdon, *Acta Mater.* 61 (2013) 7035-7059
28. R. Valiev, Y.V. Ivanisenko, E. Rauch, B. Baudelet, *Acta Mater.* 44 (12) (1996) 4705-4712
29. F. Wetscher, A. Vorhauer, R. Stock, R. Pippan, *Mater. Sci. Eng. A* 387 (2004) 809-816
30. M. Kawasaki, T.G. Langdon, *Mater. Sci. Eng. A* 498 (2008) 341-348
31. A. P. Zhilyaev, G. V. Nurislamova, B.-K. Kim, M. D. Baro, J. A. Szpunar, T. G. Langdon, *Acta Mater.* 51 (2003) 753-765
32. M. Kawasaki, S. N. Alhajeri, C. Xu, T.G. Langdon, *Mater. Sci. Eng. A* 529 (2011) 345-351
33. M. Kawasaki, *J. Mater. Sci.* 49 (2014) 18-34
34. A.P. Zhilyaev, S. Lee, G. V. Nurislamova, R. Z. Valiev, T. G. Langdon, *Src. Mater.* 44 (2001) 2753-2758
35. A. P. Zhilyaev, A. A. Gimazov, G. I. Raab, T. G. Langdon, *Mater. Sci. Eng. A* 486 (2008) 123-126
36. K. Edalati, Y. Yokoyama, Z. Horita, *Mater. Trans.* 51 (2010) 23-26
37. M. M. Castro, P. H. R. Pereira, A. Isaac, R. B. Figueiredo, T. G. Langdon, *J. Alloy. Compd.* 780 (2019) 422-427
38. A. V. Korznikov, I. M. Safarov, D. V. Laptionok, R. Z. Valiev, *Acta Metall. Mater.* 39 (1991) 3193-3197
39. V. V. Stolyarov, Y. T. Zhu, T. C. Lowe, R. K. Islamgaliev, R. Z. Valiev, *Mater. Sci. Eng. A* 282 (2000) 78-85
40. X. Sauvage, P. Jessner, F. Vurpillot, R. Pippan, *Src. Mater.* 58 (2008) 1125-1128

41. K. Kaneko, T. Hata, T. Tokunaga, Z. Horita, *Mater. Trans.* 50 (2009) 76-81
42. K. Edalati, Z. Horita, H. Fujiwara, K. Ameyama, *Metall. Mater. Trans. A* 41 (2010) 3308-3317
43. A. Bachmaier, M. Kerber, D. Setman, R. Pippan, *Acta Mater.* 60 (2012) 860-871
44. J. M. Cubero-Sesin, Z. Horita, *Mater. Sci. Eng. A* 558 (2012) 462-471
45. Y. Zhang, S. Sabbaghianrad, H. Yang, T. D. Topping, T. G. Langdon, E. J. Lavernia, J. M. Schoenung, S. R. Nutt, *Metall. Mater. Trans. A* 46A (2015) 5877-5886
46. A. P. Zhilyaev, G. Ringot, Y. Huang, J. M. Cabrera, T. G. Langdon, *Mater. Sci. Eng. A* 688 (2017) 498-504
47. Y. Huang, P. Bazarnik, D. Wan, D. Luo, P. H. R. Pereira, M. Lewandowska, J. Yao, B. E. Hayden, T. G. Langdon, *Acta Mater.* 164 (2019) 499-511
48. K. Oh-ishi, K. Edalati, H. S. Kim, K. Hono, Z. Horita, *Acta Mater.* 61 (2013) 3482-3489
49. O. Bouaziz, H. S. Kim, Y. Estrin, *Adv. Eng. Mater.* 15 (2013) 336-340
50. B. Ahn, A. P. Zhilyaev, H. -J. Lee, M. Kawasaki, T. G. Langdon, *Mater. Sci. Eng. A* 635 (2015) 109-117
51. J. -K. Han, H. -J. Lee, J. -i. Jang, M. Kawasaki, T. G. Langdon, *Mater. Sci. Eng. A* 684 (2017) 318-327
52. X. Qiao, X. Li, X. Zhang, Y. Chen, M. Zheng, I. S. Golovin, N. Gao, M. J. Starink, *Mater. Lett.* 181 (2016) 187-190
53. N. Ibrahim, M. Peterlechner, F. Emeis, M. Wegner, S. V. Divinski, G. Wilde, *Mater. Sci. Eng. A* 685 (2017) 19-30
54. L. Lutterotti, *Nucl. Instrum. Methods Phys. Res. Sect. B* 268 (2010) 334-340
55. C. Xu, H. Zenji, T. G. Langdon, *Mater. Trans.* 51 (2010) 2-7
56. K. Edalati, K. Imamura, T. Kiss, Z. Horita, *Mater. Trans.* 53 (2012) 123-127
57. K. Lu, L. Lu, S. Suresh, *Science* 324 (2009) 349-352
58. J.-K. Han, D. K. Han, G. Y. Liang, Jae-Il Jang, T. G. Langdon, M. Kawasaki, *Adv. Eng. Mater.* 20 (2018) 1800642

59. M. Kawasaki, B. Ahn, T. G. Langdon, Mater. Sci. Eng. A 527 (2010) 7008-7016
60. J.-K. Han, J.-i. Jang, T.G. Langdon, M. Kawasaki, Mater. Trans. 60 (2019) 1131-1138
61. ASM Material Data Sheet, asm.matweb.com, Retrieved 2019-10-20
62. AZo Materials Data Sheet, azom.com, Retrieved 2019-10-20